

Pseudo 3D Modeling and Analysis of the SEI Growth Distribution in Large Format Li-Ion Polymer Pouch Cells

To cite this article: Ali Awarke *et al* 2013 *J. Electrochem. Soc.* **160** A172

View the [article online](#) for updates and enhancements.

You may also like

- [Modeling Voltage Decay During Calendar-Life Aging](#)
Dongliang Lu, M. Scott Trimboli, Yujun Wang *et al.*
- [Revisiting the \$t^{0.5}\$ Dependence of SEI Growth](#)
Peter M. Attia, William C. Chueh and Stephen J. Harris
- [Electrochemical Kinetics of SEI Growth on Carbon Black: Part II. Modeling](#)
Supratim Das, Peter M. Attia, William C. Chueh *et al.*



Your Lab in a Box!

The PAT-Tester-i-16: All you need for Battery Material Testing.

- ✓ All-in-One Solution with integrated Temperature Chamber!
- ✓ Cableless Connection for Battery Test Cells!
- ✓ Fully featured Multichannel Potentiostat / Galvanostat / EIS!

www.el-cell.com +49 40 79012-734 sales@el-cell.com


electrochemical test equipment





Pseudo 3D Modeling and Analysis of the SEI Growth Distribution in Large Format Li-Ion Polymer Pouch Cells

Ali Awarke,^{a,*} Stefan Pischinger,^a and Jürgen Ogrzewalla^b

^aInstitute for Combustion Engines, RWTH Aachen University, D-52062 Aachen, Germany

^bFEV Motorentechnik GmbH, D-52078 Aachen, Germany

Today's Li-ion battery stringent requirements include high electric currents, large format cells and possibly the use of carbon based current collectors, which would enhance the electrochemical-thermal non-uniformities in the cell. Although a number of models have been implemented in order to study such non-uniformities, no efforts have been made to describe the distribution of side reaction rates and their effect on aging distribution. To fill that gap, we developed a pseudo-3D porous electrode electrochemical model that incorporates via first principles the solid-electrolyte interphase (SEI) growth on the anode, which is thought to be a dominant aging mechanism. The model was used to simulate the cyclic behavior of a large format (40 Ah) Li-ion polymer pouch cell with the assumption of a carbon based positive current collector. It was found that SEI growth localization would form in the electrode thickness and planar dimensions during discharging, but would be destroyed during the subsequent charging, so that the associated aging would be uniform upon cycling. This suggests that computationally efficient lumped models could be used to describe the cell aging process associated with the SEI growth on the graphitic anode, which would be ideal for onboard implementations such as in electric vehicle applications.

© 2012 The Electrochemical Society. [DOI: 10.1149/2.022302jes] All rights reserved.

Manuscript submitted May 18, 2012; revised manuscript received November 2, 2012. Published November 26, 2012.

Li-ion battery models, which are based on the porous electrode (PE) theory,^{1,2} are commonly resolved in the 1D thickness dimension of the electrodes, assuming that the electric potential is uniform in the plane of the current collectors. This assumption is valid as long as small format cells are the case, which is typical in laboratory work. However, in large format cells, the ohmic drop in the relatively long current collectors would affect the current distribution so that in-plane performance inhomogeneities exist. These inhomogeneities are larger at higher currents and/or badly conducting current collectors. In-plane temperature non-uniformities were for example demonstrated by using cell surface thermal images in, Refs. 3 and 4, where an asymmetric heat localization near the tabs was the case. An in-plane SOC distribution was also visualized in Ref. 5 using synchrotron X-ray micro diffraction, which hints that higher currents exist near the tab regions. In today's large scale applications such as electric vehicles, Li-ion cells are required to be operated with high currents while taking at the same time a large format with thin current collectors, which would increase inhomogeneities. Moreover, carbon based collectors⁶⁻⁸ were suggested, and a graphite positive collector have often been used⁹ in order to avoid the corrosion of the aluminum collector when using electrolytes other than hexafluorophosphate (for example Imide salts). Given their relatively bad electric conductivity, carbon based collectors are expected to enhance the inhomogeneities in full scale cells. Multi-dimensional models are thus desirable to understand the cell electric current distribution, in addition to the role of the current collector and the position of the tabs, which are critical in deciding the cost, weight and volume of the cell.

Few multi-dimensional models have been developed and used mainly to determine the temperature distribution across a large cell or module.¹⁰⁻¹⁵ The majority of the models account for spatially resolved currents caused by a temperature difference only, where the effect of the ohmic loss in the collector is not considered. Verbrugge et al.¹⁶ was the first to deal with the in-plane non-homogeneity caused by the collector ohmic loss. He assumed a secondary current distribution with linear kinetics, while a perturbation analysis was used to capture the variation in the plane of the collector. The assumptions remain nevertheless valid for short polarization times after a relaxed state. Harb et al.^{17,18} decomposed the computational domain into a 1D porous electrode model in the thickness direction of the electrodes, and a 2D model of the continuity of charge in the in-plane dimensions of the collectors. Other researchers^{4,19-22} used a similar decomposition but implemented in the 1D thickness dimension a simplified surrogate

model, such as polynomials. Srinivasan²³ solved the whole set of equations in 2D, which is a computationally expensive approach. On the contrary, a computationally efficient resistor network discretization was used in Refs. 11, 24, and 25.

The results shown in the above works suggest that an electrochemical-thermal non homogenous performance would lead to non homogeneous side reactions and aging distribution in the cell. This is especially important when replacing the aluminum current collector with a graphite based current collector. First principles based aging models, describing the distribution of aging related specific mechanisms such as the dominating SEI growth, were nevertheless so far not incorporated in such a multi-dimensional framework. In order to investigate the effect of electric current non homogeneity on side reactions and aging, we developed a pseudo-3D cell model by coupling various spatially distributed 1D PE models to the temperatures and voltages in the in-plane cell dimensions, while including a first principles based SEI growth model on the anode. A large format 40 Ah lithium polymer pouch cell from the battery manufacturer Kokam was considered and various discharge curves were used for model calibration. However, a graphite based positive current collector was assumed during the SEI growth analysis. The intention behind that is to understand how would a relatively bad conductive graphite based negative collector, such as recently suggested, affect the associated aging distribution of the cell.

Mathematical Modeling

Model setup and equations.— Due to the small thickness of the considered cell (10.7 mm), a temperature gradient in the normal dimension was neglected, which allows the use of a single cell sandwich (cathode-separator-anode) and a 2D plane cell thermal computational domain. Moreover, due to the small thickness of the current collector, a voltage gradient in its normal dimension is generally negligible, so that a 2D plane collector voltage model is valid. Accordingly, the cell electrochemical-thermal non-uniform performance was modeled in here by:

1. discretizing a single cell sandwich into 9 electrochemical sub-domains (Figure 1a) and assigning to each one a 1D dimensionless porous electrode model (Figure 1b)
2. calculating the collector (positive and negative) in-plane voltage distribution by solving the continuity of charge in the 2D collector plane electric domain (Figure 1b)
3. calculating the cell in-plane temperature distribution by solving the continuity of heat in the 2D plane cell thermal domain (Figure 1c)

*Electrochemical Society Active Member.

^zE-mail: awarke@vka.rwth-aachen.de

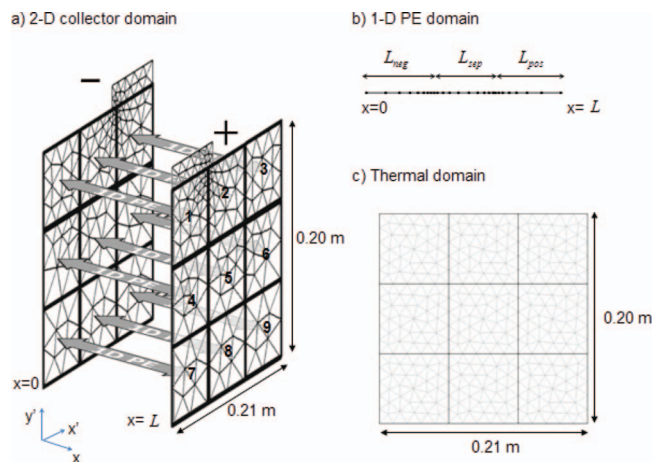


Figure 1. (a) Cell in-plane discretization of the electric potential domain (b) cell in-thickness discretization of the electrochemical domain (c) cell in-plane discretization of the thermal domain.

- assigning to each 1D PE model, voltage boundary conditions that are averaged from the collector voltage distribution in the associated collector region
- assigning to each 1D PE model, temperature fields that are averaged from the cell temperature distribution in the associated cell region

Electrolyte and solid transport.—In each k^{th} 1D PE model the distributions of the electrolyte electric potential (ϕ_e^k), electrolyte Li-ion concentration (c_e^k), solid phase electric potential (ϕ_s^k) and particle normal intercalation main current density ($j^{m,k}$) were calculated by solving the following dimensionless equations:

Conservation of charges in the electrolyte of the electrodes ($i = pos, neg$):

$$\frac{\partial i_e^k}{\partial x} = S_{a,i} j^{m,k} L_i \quad [1]$$

Conservation of charges in the electrolyte of the separator:

$$\frac{\partial i_e^k}{\partial x} = 0 \quad [2]$$

Modified Ohm's Law in the electrolyte phase ($i = pos, neg$):

$$i_e^k = -\frac{\kappa_{e,i}^{eff}}{L_i} \frac{\partial \phi_e^k}{\partial x} + \frac{2\kappa_{e,i}^{eff} RT}{L_i F} \left(1 + \frac{\partial \ln f_{\pm}}{\partial \ln c_e^k}\right) (1 - t^+) \frac{\partial}{\partial x} \ln c_e^k \quad [3]$$

Conservation of lithium mass in the electrolyte of the electrodes ($i = pos, neg$):

$$\begin{aligned} \phi_e L_i \frac{\partial c_e^k}{\partial t} + \frac{\partial}{\partial x} \left(-v_+ \frac{D_{e,i}^{eff}}{L_i} \frac{\partial c_e^k}{\partial x} \right) + \frac{i_e^k}{z_+ F v_+} \frac{\partial t^+}{\partial x} \\ = \frac{S_{a,i} j^{m,k} L_i}{z_+ F v_+} (1 - t^+) \end{aligned} \quad [4]$$

Conservation of lithium mass in the electrolyte of the separator ($i = sep$):

$$\phi_e L_i \frac{\partial c_e^k}{\partial t} + \frac{\partial}{\partial x} \left(-v_+ \frac{D_{e,i}^{eff}}{L_i} \frac{\partial c_e^k}{\partial x} \right) + \frac{i_e^k}{z_+ F v_+} \frac{\partial t^+}{\partial x} = 0 \quad [5]$$

Conservation of charges in the solid phase of the electrodes ($i = pos, neg$):

$$i_s^k = -\frac{\kappa_{s,i}^{eff}}{L_i} \frac{\partial \phi_s^k}{\partial x} \quad [6]$$

$$\frac{\partial}{\partial x} (i_s^k) = -S_{a,i} j^{m,k} L_i \quad [7]$$

Bulter-Volmer reaction rate at the electrode-electrolyte interface ($i = pos, neg$):

$$j^{m,k} = j_{0,i}^m \left\{ \exp \left[\frac{0.5 F \eta^{m,k}}{RT} \right] - \exp \left[-\frac{0.5 F \eta^{m,k}}{RT} \right] \right\} \quad [8]$$

Reaction overpotential ($i = pos, neg$):

$$\eta^{m,k} = \phi_s^k - \phi_e^k - U_{eq,neg} (\theta_{surf}^k) - j^{m,k} S_{a,neg} R_{SEI}^k \quad [9]$$

Irreversible SEI growth.—In order to consider the capacity fade due to the growth of the anode SEI, an approach based on the single particle analysis of Ning et al.²⁶ was used with the following assumptions:

- The electrolyte solvent reduction on the anode is the main contributor to the SEI growth
- Even though an isolating layer has been formed, the continuous reduction of the electrolyte with further cycling is still possible due to the existence of pores in the SEI material
- The SEI products are insoluble salts (assumed in this work to be dilithium ethylene dicarbonate) that cannot disassociate back to give lithium ions, making thus the side reaction fully irreversible
- Enough solvent is available for the reduction reaction, i.e. There is no limitation due to the consumption of the solvent

The total reduction current at the anode was split into a main intercalation current (j^m) and a side reaction current (j^{side}) accounting for the electrolyte reduction and modeled by the Tafel equation:

$$j^{side,k} = j_0^{side} \exp \left(-\frac{0.5 F}{RT} \eta^{side,k} \right) \quad [10]$$

with the following side reaction overpotential:

$$\eta^{side,k} = \phi_s^k - \phi_e^k - U_{eq,neg}^{side} - j^{side,k} S_{a,neg} R_{SEI}^k \quad [11]$$

The irreversible loss of lithium in a cycle was estimated by integrating the side reaction current over the time of one discharge-charge cycle:

$$dQ_s^k = \int_{cycle} j^{side,k} S_n dt \quad [12]$$

The dimensionless capacity loss, i.e., change in the reference stoichiometric coefficient was calculated according to:

$$d\bar{Q}_s^k = \frac{dQ_s^k}{A_c L_{neg} \Phi_{AM,neg} c_{s,neg}^{sat} F} \quad [13]$$

In addition to changes in the stoichiometric coefficients, film buildup occurs adding to the interfacial current resistance used in Eq. 11. The rate of increase of the thickness of the film was estimated from the irreversible inward flux of lithium, assuming a homogeneous layer formation:

$$\frac{\partial \delta_{SEI}^k}{\partial t} = -\frac{j^{side,k} M_{SEI}}{\rho_{SEI} F} \quad [14]$$

where M and ρ_{SEI} are the molecular weight and density of the SEI layer respectively. The interfacial resistance increment per cycle associated with a given thickness was calculated from the electrical conductivity of the layer using:

$$dR_{SEI}^k = \int_{cycle} \frac{\partial \delta_{SEI}^k}{\partial t} \frac{1}{\kappa_{SEI}} dt \quad [15]$$

In order to simulate efficiently the capacity fade for a large number of cycles (~ 1000), a single cycle was simulated during which the increment in the dimensionless capacity loss (Eq. 13) and the SEI resistance (Eq. 15) were evaluated. The rate of the reduction side reaction was then assumed to remain constant for N_{cycle}^{cst} number of cycles, so that at the end of the $m \times N_{cycle}^{cst}$ cycle the reference stoichiometric coefficient and the interfacial resistance could be updated using:

$$R_{SEI}^k \Big|_{m \times N_{cycle}^{cst}} = R_{SEI}^k \Big|_{(m-1) \times N_{cycle}^{cst}} + dR_{SEI}^k N_{cycle}^{cst} \quad [16]$$

$$\bar{Q}_s^k \Big|_{m \times N_{cycle}^{cst}} = \bar{Q}_s^k \Big|_{(m-1) \times N_{cycle}^{cst}} + d\bar{Q}_s^k N_{cycle}^{cst} \quad [17]$$

The process repeats itself until the required number of cycles is reached. In this work $N_{cycle}^{cst} = 100$ was used as a good compromise between accuracy and computational efficiency.¹

Solid diffusion.—Using a full particle diffusion model to solve the distribution of the solid phase lithium ion concentration (c_s) would lead to an increased modeling setup and computational effort. Alternatively, the parabolic polynomial approximation approach suggested in Refs. 28 and 29, was implemented as follows:

The concentration profile inside the particle was estimated to:

$$c_s^k = a_1 + a_2 r^2 + a_3 r^4 \quad [18]$$

So that the average ($c_{s,av}$) and the surface solid concentrations ($c_{s,surf}$) can be calculated using:

$$\frac{\partial c_{s,av}^k}{\partial t} = -\frac{3}{r_p F} j^{m,k} \quad [19]$$

$$\frac{d\bar{q}_s^k}{dt} + 30 \frac{D_s}{r_p^2} \bar{q}_s^k + \frac{45}{2} \frac{j^{m,k}}{F r_p^2} = 0 \quad [20]$$

$$\frac{35 D_s}{r_p} (c_{s,surf}^k - c_{s,av}^k) - 8 D_s \bar{q}_s^k = -\frac{j^{m,k}}{F} \quad [21]$$

where \bar{q}_s^k is the volume average concentration flux.

The resulting estimated solution was shown accurate enough in Ref. 30 when compared to the exact solution. The parabolic approximation approach requires the use of a constant solid diffusion coefficient leading to a modeling limitation, which is however judged acceptable in this work.

Temperatures.—The in-plane temperature distribution (T) was evaluated by solving the following heat equation (non-dimensional) in the thermal domain:

$$h_{cell} \rho_{cell} C^{eff} \frac{dT}{dt} = \lambda_p^{eff} \left(\frac{\partial^2 T}{\partial x^2} + \frac{\partial^2 T}{\partial y^2} \right) + \dot{Q}_{rxn}^k + \dot{Q}_{rev}^k + \dot{Q}_{Ohm}^k \quad [22]$$

\dot{Q}_{rxn}^k , \dot{Q}_{rev}^k and \dot{Q}_{Ohm}^k are the heat sources in the k^{th} sub-domain representing respectively interfacial reactions, entropy changes and ohmic losses, which are averaged and mapped from the k^{th} associated 1D dimensionless PE model using:

$$\dot{Q}_{Ohm}^k = \frac{1}{L_{neg} + L_{pos} + L_{sep}} \times \left\{ \begin{aligned} & \int_0^1 \left[\frac{\kappa_s^{eff}}{L_{neg}^2} \left(\frac{\partial \varphi_s^k}{\partial x} \right)^2 + \frac{\kappa_e^{eff}}{L_{neg}^2} \left(\frac{\partial \varphi_e^k}{\partial x} \right)^2 - \frac{2\kappa_e^{eff} RT^k}{L_{neg}^2 F} (1-t^+) \left(1 + \frac{\partial \ln f_{\pm}}{\partial \ln c_e} \right) \frac{\partial (\ln c_e^k)}{\partial x} \frac{\partial \varphi_e^k}{\partial x} \right] L_{neg} \cdot dx \\ & + \int_0^1 \left[\frac{\kappa_s^{eff}}{L_{sep}^2} \left(\frac{\partial \varphi_s^k}{\partial x} \right)^2 - \frac{2\kappa_e RT^k}{L_{sep}^2 F} (1-t^+) \left(1 + \frac{\partial \ln f_{\pm}}{\partial \ln c_e} \right) \frac{\partial (\ln c_e^k)}{\partial x} \frac{\partial \varphi_e^k}{\partial x} \right] L_{sep} \cdot dx \\ & + \int_0^1 \left[\frac{\kappa_s^{eff}}{L_{pos}^2} \left(\frac{\partial \varphi_s^k}{\partial x} \right)^2 + \frac{\kappa_e^{eff}}{L_{pos}^2} \left(\frac{\partial \varphi_e^k}{\partial x} \right)^2 - \frac{2\kappa_e RT^k}{L_{pos}^2 F} (1-t^+) \left(1 + \frac{\partial \ln f_{\pm}}{\partial \ln c_e} \right) \frac{\partial (\ln c_e^k)}{\partial x} \frac{\partial \varphi_e^k}{\partial x} \right] L_{pos} \cdot dx \end{aligned} \right. \quad [23]$$

$$\dot{Q}_{rxn}^k = \frac{1}{L_{sep} + L_{neg} + L_{pos}} \left[\int_0^1 S_{a,neg} j^{m,k} \eta^{m,k} L_{neg} \cdot dx + \int_0^1 S_{a,pos} j^{m,k} \eta^{m,k} L_{pos} \cdot dx \right] \quad [24]$$

¹The value of $N_{cycle}^{cst} = 100$ was judged suitable by comparing the resulting SEI thickness evolution with that resulting from using $N_{cycle}^{cst} = 10$ and finding a negligible change.

$$\dot{Q}_{rev}^k = \frac{1}{L_{sep} + L_{neg} + L_{pos}} \left[\int_0^1 S_{a,neg} j^{m,k} T \frac{\partial U_{eq,neg}}{\partial T} L_{neg} \cdot dx + \int_0^1 S_{a,pos} j^{m,k} T \frac{\partial U_{eq,pos}}{\partial T} L_{pos} \cdot dx \right] \quad [25]$$

The in-plane thermal conductivity (λ_p^{eff}) and effective specific heat capacity (C^{eff}) were identified from thermal tests to be $1.2 \text{ W m}^{-1} \text{ K}^{-1}$ and $931 \text{ J K}^{-1} \text{ Kg}^{-1}$ respectively.

Collector voltage distribution.—The voltage distribution in the collector was determined by solving the continuity of charge equations (dimensional) in the positive and negative 2D collector voltage domains:

$$\frac{\partial i_{x'}^{pc}}{\partial x'} + \frac{\partial i_{y'}^{pc}}{\partial y'} = J^{pc} \quad [26]$$

$$\frac{\partial i_{x'}^{nc}}{\partial x'} + \frac{\partial i_{y'}^{nc}}{\partial y'} = J^{nc} \quad [27]$$

where,

- i^{pc} and i^{nc} refer to the positive and negative collector current density (A m^{-2}) respectively
- J^{pc} and J^{nc} are the positive and the negative collector current sources (A m^{-2}) respectively
- x' and y' refer to the dimensions in the collector domain

Ohm's Law was used in order to express the current flux as:

$$i_{x'}^{pc} = -\kappa^{pc} L^{pc} \frac{\partial \varphi^{pc}}{\partial x'}, i_{y'}^{pc} = -\kappa^{pc} L^{pc} \frac{\partial \varphi^{pc}}{\partial y'} \quad [28]$$

$$i_{x'}^{nc} = -\kappa^{nc} L^{nc} \frac{\partial \varphi^{nc}}{\partial x'}, i_{y'}^{nc} = -\kappa^{nc} L^{nc} \frac{\partial \varphi^{nc}}{\partial y'} \quad [29]$$

Where κ and L are the electrical conductivity and the thickness of the collector respectively. The current source in the current collector

associated with the k^{th} 1D PE model was calculated as:

$$J^{pc} = -\frac{\kappa_s^{eff}}{L_{pos}} \frac{\partial \varphi_s^k}{\partial x} \Big|_{x=L_{pos}+L_{neg}+L_{sep}} \quad [30]$$

$$J^{nc} = \frac{-\kappa_s^{eff}}{L_{neg}} \frac{\partial \varphi_s^k}{\partial x} \Big|_{x=0} \quad [31]$$

The voltage of the cell was calculated as the positive tab voltage minus an ohmic drop to account implicitly for unconsidered

resistances such as that of the collector-electrode contact:

$$E_{cell} = \varphi^{pc}|_{tabs} - \frac{I}{n_{layer}} R_{lumped} \quad [32]$$

Boundary conditions.—The following boundary conditions were applied.

lithium salt flux insulation at the collector-electrolyte interface:

$$\left. \frac{\partial c_e^k}{\partial x} \right|_{x=Lsep+Lpos+Lneg} = \left. \frac{\partial c_e^k}{\partial x} \right|_{x=0} = 0 \quad [33]$$

$$\left. \frac{\partial \varphi_s^k}{\partial x} \right|_{x=Lsep+Lpos+Lneg} = \left. \frac{\partial \varphi_s^k}{\partial x} \right|_{x=0} = 0 \quad [34]$$

Insulation to an electric current flux at the electrode-separator interface:

$$\left. \frac{\partial \varphi_s^k}{\partial x} \right|_{x=Lneg} = \left. \frac{\partial \varphi_s^k}{\partial x} \right|_{x=Lsep+Lneg} = 0 \quad [35]$$

The average collector potential value in each k^{th} 2D sub-domain was input as a Dirichlet boundary condition in its associated 1D PE model:

$$\varphi_s^k|_{x=Lneg+Lsep+Lpos} = \frac{1}{A_c^k} \int_{A_c^k} \varphi^{pc} dA \quad [36]$$

$$\varphi_s^k|_{x=0} = \frac{1}{A_c^k} \int_{A_c^k} \varphi^{nc} dA \quad [37]$$

φ^{pc} and φ^{nc} are the potential distributions in the positive and negative collector planes respectively and the integral is taken over the area of each sub-domain.

A Neumann boundary condition with a zero flux was applied on all collector boundaries except at the tabs. A zero Dirichlet boundary condition was applied on the negative tab:

$$\varphi^{nc} = 0 \quad [38]$$

while the following Neumann boundary condition was applied on the positive tab to consider the cell loading:

$$-\kappa^{pc} L^{pc} \frac{\partial \varphi^{pc}}{\partial y'} = \frac{I}{n_{layer} W_{tab}} \quad [39]$$

In the above I is the cell current (positive on discharge), n_{layer} is number of cell sandwiches and W_{tab} is the length of the tab section.

Solution procedures.—The above equations were implemented in the FE software COMSOL 3.5a using 8 coupled PDE general form application modes. A damped Newton's method was selected for the non-linear solver with the default damping parameters, while the backward differentiation formula (BDF) was used for the time integration. The linearized system was solved using the Direct (UMFPACK) solver. More information can be found in.³¹

Model calibration.— In order to validate the above model, the parameters were adjusted using a three-step procedure as follows. The considered Kokam cell contains $\text{LiNi}_{1/3}\text{Mn}_{1/3}\text{Co}_{1/3}$ and graphite as the cathode and anode active materials respectively. A LiPF_6 salt in an EC/EMC solvent mixture and a PVDF polymer matrix are used for the gel electrolyte. The associated intrinsic material properties were obtained in the first step from commonly used values in the literature. In the second step, the reference stoichiometric coefficients, porosities and collector contact area were identified using a Bayesian inference scheme, which extracts a probability distribution function of the variables from information about the cell OCP, percentage of Li-ion consumed in the SEI formation cycle and the thickness of the cell. The most probable parameter values were then selected and used afterwards. In the third step, the remaining model parameters, which are related to the overpotential exhibited in the cell, were characterized

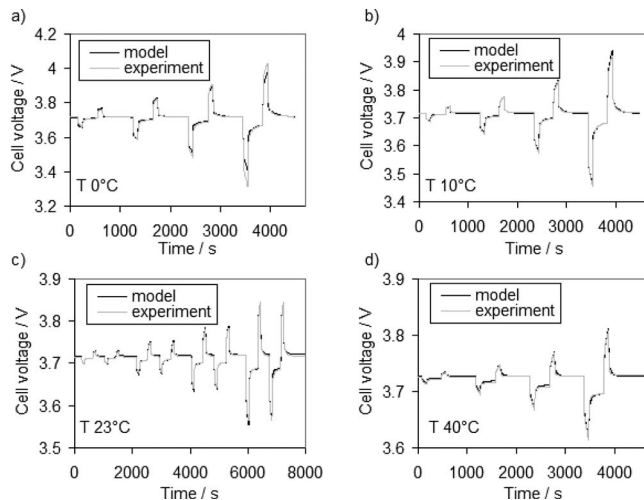


Figure 2. Comparison between model and measured response during the pulse test at SOC = 50% and various temperatures.

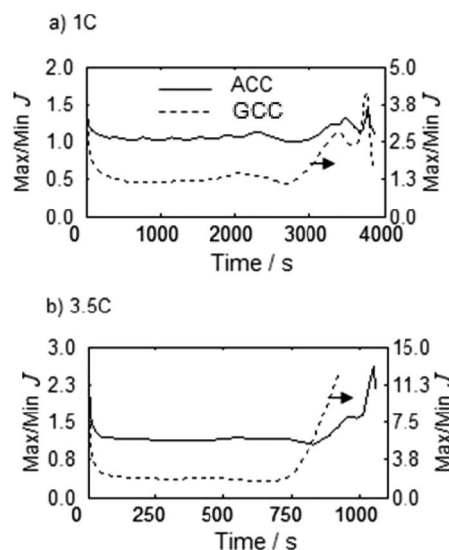


Figure 3. Ratio of maximum to minimum values for the collector current source during a (a) 1 C and (b) 3.5 C discharge (room temperature initial conditions).

by fitting the model voltage response to voltage measurements taken during a pulse test at different SOC and temperatures. The fit is shown in Figure 2 at different temperatures for SOC = 50%, which has a good quality with a minor deterioration in the high rate / overpotential regions at 0°C. More details regarding the model calibration process can be found in Appendix.

Model use.— Previous works have shown that localization occurs near the tabs and increases with the electrical resistance of the current collectors.^{4,16,19–22} Localization effects would thus be important when replacing aluminum positive collectors (ACC) with graphite current collectors (GCC) such as GTY grade Grafoil, RTM foil from UCAR Carbon Co. Inc. which was suggested in Ref. 9. This effect is elaborated in Figures 3 and 4. Notice how in Figure 3, the non-uniformity factor² of the collector current source is well above unity especially when using a graphite current collector and higher cell currents. The increase of non-uniformity at the end of discharge corresponds to the

²Non-uniformity factor refers to the ratio of the maximum to the minimum value in a distribution.

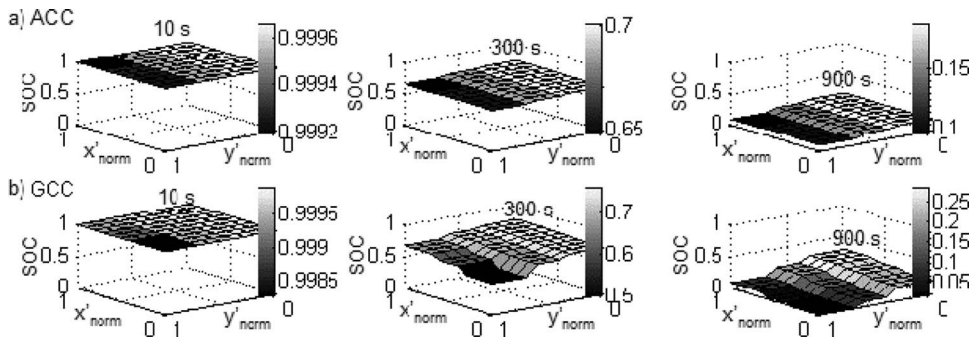


Figure 4. In-plane SOC distribution (positive tab at $x'_{\text{norm}} = 0$, $y'_{\text{norm}} = 1$) during a 3.5 C discharge with room temperature initial conditions.

depletion of the cell region near the tabs and the shift of the current toward regions away from the tabs. This is elaborated in the SOC distribution shown in Figure 4. A GCC cell refers in this work to a virtual cell using the above graphite current collector with a thickness of 75 μm and conductivity of $1.25\text{e}5 \text{ S m}^{-1}$.⁹ (all other parameters remaining fixed as after calibration).

Given the above previous observations, it would be interesting to know the effects of severe localization (such as in the GCC cell case) on side reactions and their associated cell aging. As the electrolyte reduction on the anode and its associate SEI growth is a dominant cell aging mechanism, its analysis was considered in here. Observations of the in-cell aging distribution throughout the cell lifetime are mainly in focus. A loading cycle was selected and consisted of 1) a discharge phase from an end of charge voltage (EOCV) to a lower cutoff voltage (EODV), followed immediately by 2) a constant current (CC) charging phase till the upper cutoff voltage (EOCV) is reached after which 3) a constant voltage (CV) charging regime occurs till the lower cutoff current (EOCC) is reached. The current and voltage profiles within a cycle are shown in Figure 5. The in-thickness as well as in-plane capacity fade distribution were analyzed assuming a GCC cell and various rates including 1 C/3.5 C discharging and 1 C/2 C charging currents.

Results and Discussion

The anode in-thickness distribution is considered first and elaborated in Figure 6 using a 1 C charging/discharging rate and room temperature conditions during the considered loading cycle. It can be observed in Figure 6a that the reduction side reactions are slightly lower near the separator during the discharge time between 0 s and 3834 s.

This is emphasized in Figure 6b where the spatial profiles are shown at discrete times. A gradient in the electrolyte electric potential exists during discharge and is consistent with the lithium ions migration toward the cathode, i.e., the electrolyte electric potential is higher at the negative collector side and decreases in the direction of the separator. On the other hand, due to a relatively good electrical conductivity in the solid phase, the solid electric potential does not form

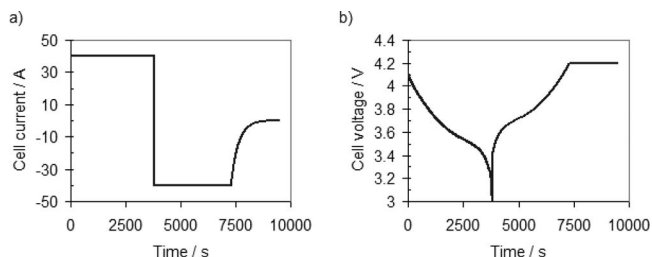


Figure 5. (a) Current profile and (b) voltage profile in the considered loading cycle.

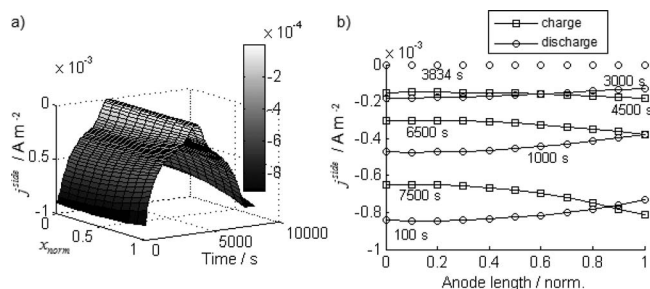


Figure 6. Side reaction current distribution in the anode thickness direction during the reference loading cycle (a) variation of the profile with time (b) profile at various discrete times. ($x_{\text{norm}} = 0$ corresponds to collector side).

considerable gradients. Accordingly, the side reaction overpotential (Eq. 8-4) is more positive at the separator side resulting in slower side reactions. The situation is reversed during charging, where the electrolyte potential gradient results in a more positive overpotential at the collector side. As result, the reduction side reactions at the collector side, which are enhanced during discharging, are slowed down during the CC charging as clarified in Figure 7a. The associated aging non-homogeneity that is developed during discharging is thus mitigated during charging, so that at the end of a cycle a uniform capacity loss is the case (Figure 7b).

In the following in-plane analysis the distribution in the anode thickness direction is not considered and quantities averaged over the negative electrode thickness are used. Figure 8 shows the behavior of the sub-domains corresponding to $k = 1$ and $k = 9$, which represent the regions nearest to the tabs and farthest from the tabs respectively. Since the current flows upon discharge from the positive to the negative current collector, the tab regions experience the lowest potentials in the positive collector and the highest potentials in the negative collector. The situation is reversed during charging, which leads to the local cell voltages and the solid potentials w.r.t the electrolyte shown in Figure 8a and 8b. As a result, the reduction side reaction evolves spatially in a way similar to the in-thickness profile,

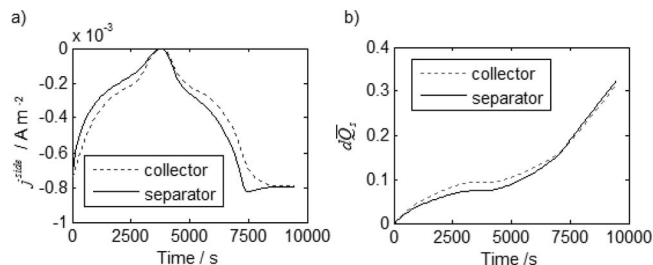


Figure 7. Comparison between (a) the side reaction current and (b) the irreversible capacity loss at the collector and separator side during a cycle.

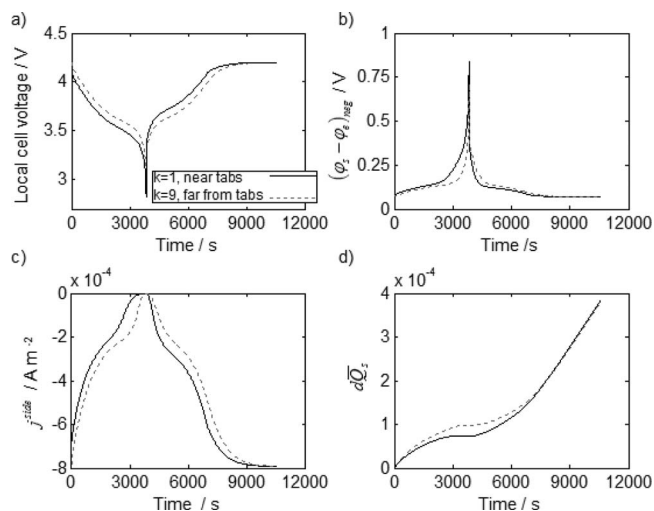


Figure 8. (a) Cell voltage (b) negative potential w.r.t. electrolyte (c) side reaction current and (d) dimensionless capacity loss near the tabs ($k = 1$) and far from the tabs ($k = 9$).

i.e., lower near the tabs / higher far from the tabs during discharging, and higher near the tabs / lower far from the tabs during charging (Figure 8c). Although a non-uniform capacity fade is the case at the end of discharging (Figure 8d), the non-uniformity is destroyed at the end of the cycle. Figure 8 shows the electrochemical behavior of the two cell regions ($k = 1$ and $k = 9$) which exhibited the highest difference. In order to elaborate the distribution among the remaining electrochemical discretization sub-domains, Figure 9 shows the distribution of the negative potential and side reaction current near the middle of discharging (Figure 9a and 9b) and charging (Figure 9c and 9d). In addition to a longitudinal gradient, there is a lateral gradient which is also reversed upon current reversal, resulting in a homogeneous capacity fade in the lateral dimension as well.

The previous results demonstrate how higher currents would enhance non-homogeneous electrochemical reactions, which suggest the following hypothesis: increasing separately either the discharging or the charging rate would enhance the inhomogeneous capacity fade at the end of a full cycle. The hypothesis was tested by increasing either the discharging current to a 3.5 C (140 A) or the charging current to 2 C (80 A). The same capacity fade distribution trends as above were still obtained (Figure 10a and 10b).

The evolution of the voltage curves of the considered regions ($k = 1, k = 9$) are shown in Figure 11a for the 1st, 500th and 1000th cycle. Notice how the cell voltage deviation upon aging is similar in both cell regions, which suggests that the tab effect does not contribute to a localized anode SEI related aging. This is also confirmed in Figure 11b which shows how the evolution of the dimensionless capacity loss and the SEI resistance with number of cycles for both regions are quasi super-imposed.

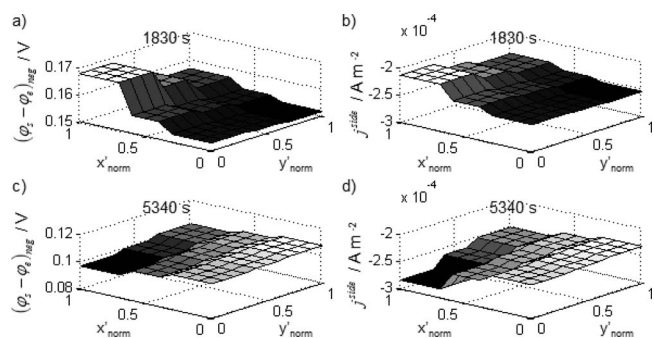


Figure 9. Distribution of negative potential w.r.t. electrolyte and side reaction current at (a, b) 1830 s (in discharge) and (c, d) 5340 s (in charge). Positive tab is located at (0,1).

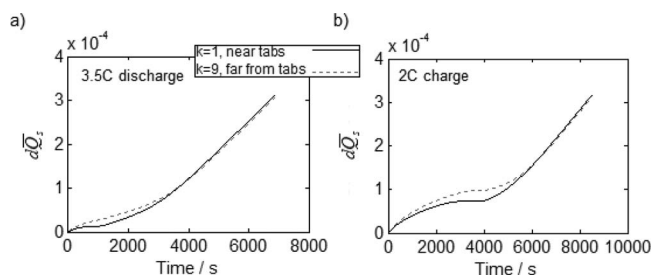


Figure 10. Dimensionless capacity fade at (a) 3.5C discharge rate and (b) 2C charge rate.

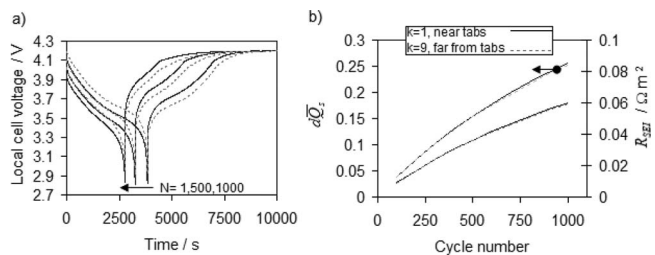


Figure 11. (a) Local cell voltages during 1st, 500th and 1000th loading cycle (b) evolution of the dimensionless capacity fade and SEI resistance over 1000 cycles.

capacity loss and the SEI resistance with number of cycles for both regions are quasi super-imposed.

Conclusions

The effect of non-uniform electric currents on the anode SEI growth distribution in Li-ion cells was analyzed in this work. A multidimensional pseudo-3D porous electrode model incorporating first principles SEI growth equations was developed for that purpose. A commercial 40 Ah large format lithium polymer pouch cell was considered for model calibration, while a graphite based positive current collector was assumed (instead of the actual aluminum one) during the SEI growth analysis. Graphite based collectors have been recently suggested and it would be worth to understand how would the induced severe electric current localization affect the associated aging distribution of the cell.

It was found that the electrolyte reduction side reaction was lowest near the cell tabs during discharging but highest during charging. A similar observation was made for the thickness direction, where the electrolyte reduction side reaction was lowest near the separator during discharging but highest during charging. As a result, the non-homogeneous SEI growth that would take place during a half cycle would be destroyed in the remaining half of the cycle. Accordingly, the SEI growth at the end of a discharging-charging cycle and thus during the cell cycle-lifetime is expected to be homogeneous, even when using a badly conducting current collector with relatively high currents (3.5 C). These findings hint also that a 1D single particle model, which has advantages in terms of computational efficiency and thus its implementation in a BMS, could be used to replicate the SEI growth based aging of a cell. However, a temperature dependency of the SEI growth was not considered in this work since relevant parameters or characterizing tests were not given. If the temperature remains high near the tabs independently of the sign of the cell current, the SEI growth in those regions could actually be favored. A further analysis incorporating a temperature dependent SEI growth model as well as experimental investigations would be helpful in backing up the findings in this study.

Table A-1. Parameters estimated from the literature / cell and solid phase properties.

Symbol	Description	Positive	Negative
AM wt%	Active material weight fraction	0.8	0.9
κ_s^{eff}	Solid phase conductivity ($S m^{-1}$)	100	
c_s^{sat}	Maximum solid phase concentration ($mol m^{-3}$)	49500 ⁴¹	30555 ^{42,43}
D_s	solid phase Li diffusion coefficient ($m^2 s^{-1}$)	0.8E-13 ³⁴	8.8E-14 ⁵⁶
r_p	Particle radius (m)	0.7E-06 ³⁴	12.5eE06 ^{44,45}
U_{eq}	Equilibrium potential	6.0826 – 6.99220 + 7.10620 ² – 0.54549E-04 exp(124.230 – 114.2593) – 2.5947 θ^{33}	122.12 θ^6 – 321.81 θ^5 + 315.59 θ^4 – 141.26 θ^3 + 28.218 θ^2 – 1.9057 θ + 0.0785 ⁴⁶
$\frac{dU_{eq}}{dT}$	Entropic coefficient	–190.34 θ^6 + 733.46 θ^5 – 1172.6 θ^4 + 995.88 θ^3 – 474.04 θ^2 + 119.72 θ – 12.457 ^{46a}	–58.294 θ^6 + 189.93 θ^5 – 240.4 θ^4 + 144.32 θ^3 – 38.87 θ^2 + 2.8642 θ + 0.1079 ⁴⁶
S_a	Electrode surface area ($m^2 m^{-3}$)		$\frac{3(1-\phi_e)}{r_p}$
$L^{nc/pc}$	Collector thickness (m)	25E-06	12E-06
$\kappa^{nc/pc}$	Collector conductivity ($S m^{-1}$)	3.5E07	5.96E07

^aProperty corresponding to LiNiCoO₂

Acknowledgment

The authors thank Dr. Jasper Vrugt for providing the DREAM algorithm used in the Bayesian inference based parameter estimation approach. The valuable comments of Dr. Robert Spotnitz are also appreciated.

Appendix: Model calibration

The model parameters were adjusted by 1) searching in the literature for commonly used values, 2) using a Bayesian inference approach and 3) fitting the model response to voltage measurements during a pulse current test at various SOC and temperatures.

Literature values

Selected parameter values that were commonly used elsewhere are shown in Table A-1. It was obvious from³² that the positive and negative active materials of the considered cell are LiNi1/3Mn1/3CO1/3 (NMC) and LiC6 respectively. The commonly used electrode AM:CB:PVDF weight composition of 0.8:0.1:0.1 in the cathode and AM:PVDF weight composition of 0.9:0.1 in the anode were assumed. The solid phase electric conductivities were set high enough after³³ in order not to play any role, since the electrodes are expected to be conductive enough not to play a considerable polarization role at the considered rates. There has been a scatter in the measured and used values of the solid diffusion coefficients in the literature, so that selecting a unique value for each electrode would be ambiguous. The values identified in Ref. 34 for the cathode and in Ref. 35 for the anode were tentatively favored as reliable sources since they were recent and extensively based on experiments. The electrode specific areas were calculated assuming spherical particles.

Table A-2. Electrolyte properties.

Symbol	Description	Value
D_e	Electrolyte phase diffusion coefficient ($m^2 s^{-1}$)	exp(-4.43-54/(T-(229+5E-03c _e))- 2.2E-04c _e)
κ_e	Electrolyte phase ionic conductivity ($S m^{-1}$)	1E-04c _e /-10.5+0.074T-0.696E-04T ² +0.668E-03c _e -0.178E-04Tc _e +0.28E-07T ² c _e +0.494E-06c _e ² -0.8861E-09c _e ² T ²
$\frac{\partial \ln f_{\pm}}{\partial \ln c_e}$	Electrolyte phase thermodynamic factor	0.601-0.24(1E-03c _e) ^{0.5} +0.982(1-0.0052(T-294))(1E-03c _e) ^{1.5}
t^+	Electrolyte phase transference number	0.38
$c_{e,0}$	Initial electrolyte concentration ($mol m^{-3}$)	1200

It can also be inferred from³² that a LiFP6 salt, a EC/EMC solvent mixture and a PVDF polymer matrix were used for the gel electrolyte. The complete data set measured in³⁶ was also tentatively used (Table A-2), knowing that the considered solvent is slightly different. In gelled electrolytes, the solvent-salt liquid mixture lies in a polymer matrix. Deducing the effective transport based on the apparent volume fraction of the electrolyte in the polymer matrix cannot be directly done using the Bruggeman relation with a 1.5 Bruggeman exponent due to 1) a solvation of the polymer by the solvent, 2) an increased tortuosity and 3) a solvent-polymer interaction. An adjusted Bruggeman exponent (b_e) was thus identified in here from measured voltage data as shown later in this appendix.

There are several possible scenarios for the side reaction between lithiated carbon and electrolyte solvent and the current state of the art does not contain any specific information regarding the insoluble products. The SEI growth parameters were thus roughly estimated in this work as shown in Table A-3. A value of 0.4 V was used for the equilibrium potential of the reduction side reaction which was used in most works.^{26,27,37-39} While the exact composition of the SEI depends on the electrolyte and AM, the presence of amorphous lithium alkyl carbonates has been observed for the majority of carbonate-based electrolytes.⁴⁰ In this work, dilithium ethylene carbonate (Li2EDC) was assumed to be the major SEI component and the properties calculated using molecular dynamics simulations in Ref. 40 were used. Exchange current density values based on experimental investigations were not found in the Literature and a value of 12.5E-07 A m⁻² was selected to result in a SEI layer thickness in the order of 10 nm after 1000 cycles.

Bayesian inference

The reference Lithium stoichiometric coefficients θ_i^{ref} (at SOC = 1), electrode porosities, electrode thicknesses and collector-electrode area were identified using a Markov Chain Monte Carlo (MCMC) simulation based Bayesian inference scheme. The above parameters are system dependent and thus cannot be obtained directly from the literature, but can be inferred from known associated facts. The statistical Bayesian inference scheme⁴⁷ uses a posterior probability density function to express the belief that a parameter has a certain value, after considering the known facts. The parameters are thus treated as random variables that cannot be determined exactly but are characterized by a prior pdf which expresses the belief/uncertainty about a parameter before examining the experimental data. Monte Carlo based numerical methods were often used to evaluate the posterior pdf and the recently developed DREAM algorithm⁴⁸ was used in here.

Table A-3. Parameter values used in the SEI growth model.

Symbol	Description	Value
$U_{eq,neg}^{side}$	Side reaction equilibrium potential, V	0.4
j_0^{side}	reduction reaction exchange current density, A m ⁻²	12.5E-07
M_{SEI}	SEI Molecular weight, Kg mol ⁻¹	0.162
ρ_{SEI}	SEI density, Kg m ⁻³	1690
κ_{SEI}	SEI electric conductivity, S m ⁻¹	5E-06
$R_{SEI,0}$	initial SEI resistance, Ωm^2	1E-03

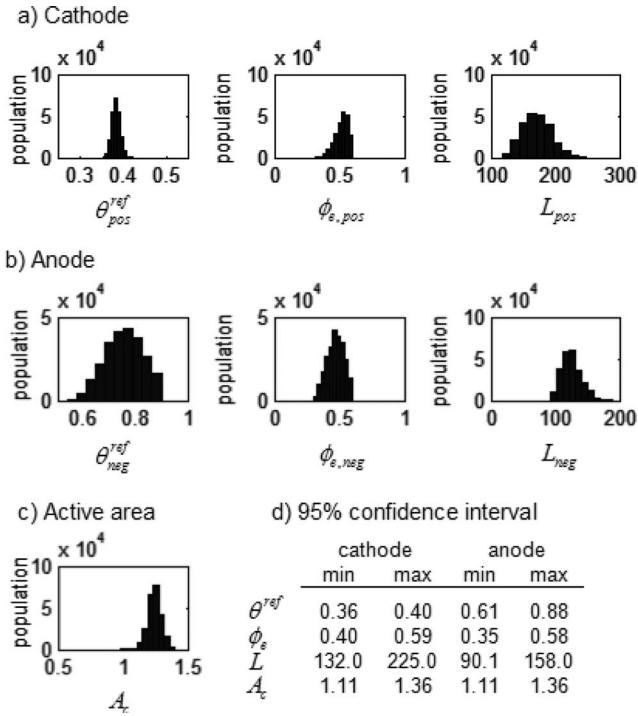


Figure A-1. Bayesian posterior distribution of (a) the cathode parameters (b) the anode parameters (c) the collector-electrode contact area and (d) the associated 95% confidence interval.

The following facts were used in order to obtain a probability density function (pdf) for the considered variables:

1. The OCP of the cell at SOC = 1 is 4.2 V
2. The OCP of the cell at SOC = 0 is 2.7 V
3. The OCP of the cell at various SOCs is equivalent to the relaxed voltage in the pulse current test at the considered SOC
4. The percentage of Lithium consumed in the SEI formation at the anode lies between 8% and 15% of the total mass of Lithium initially present in the cathode⁴⁹
5. The thickness of the stack is 10.7 mm as stated in the supplier specification sheet⁵⁰

Mathematical equations describing the above facts were used to construct an objective function that is used to generate a sample of 250000 set of parameters. The resulting parameter distribution is shown in Figure A-1 in addition to the 95% confidence interval. Due to a correlation between the parameters, a unique solution is not the case. Nevertheless, a belief that a parameter exists in a given range could be obtained as specified in the 95% confidence interval. Notice how the positive stoichiometric reference coefficient (θ_p^{ref}) is well defined within a relatively small interval. This is due to the fact that at high SOC, the negative potential is near zero so that the cell OCP is solely defined by the positive equilibrium potential which is defined by θ_p^{ref} .

To the contrary and for the same reason, the negative stoichiometric coefficient is ill conditioned. Parameter identification of PE models remains till today a major challenge and an analysis such as presented above could help quantify the amount of uncertainty hidden in the results but remains out of the scope of this work. The most probable

Table A-4. Parameters estimated from the Bayesian inference algorithm.

Symbol	Description	Positive	Separator	Negative
L_i	Thickness (m)	165E-06	30E-06 ³	103E-06
ϕ_e	Porosity	0.53	0.4 ⁴	0.51
θ_i^{ref}	reference stoichiometric coefficient	0.39	N/A	0.89
A_c	Total collector-electrode contact area (m ²)	1.34		

Table A-5. Parameters estimated by model fitting to pulse test data.

Symbol	Description	Value
R_{lumped}	ohmic resistance (Ω)	8E-04
b_e	Electrolyte phase Bruggeman constant	1.82
$j_{0,i}^m$	exchange current density (A m ⁻²)	1E-21exp(0.173T) (i = pos) 2E-21exp(0.1725T) (i = neg)

parameter values (values with the highest densities) are thus used in the remaining procedures (Table A-4).

Model fit to test data

The remaining parameters (Table A-5) were identified by fitting the model response to voltage data taken during various pulse tests, while keeping the previously found parameters constant. The pulse tests were carried out by a third party as follows. For different ambient temperatures (0°C, 10°C, 23°C, 40°C) and SOC levels, a set of 100 s pulse currents of varying magnitude (0.5C, 1C, 2C) and directions were applied in a way to maintain the desired SOC level. The SOC level was then decreased using a 1C current (40 A) applied for either 6 or 12 min. In addition to the electric potential, the cell temperature was also monitored, and the ambient one was adjusted to compensate for the cell internal heating. The voltage data and the resulting model fit can be seen in Figure A-2.

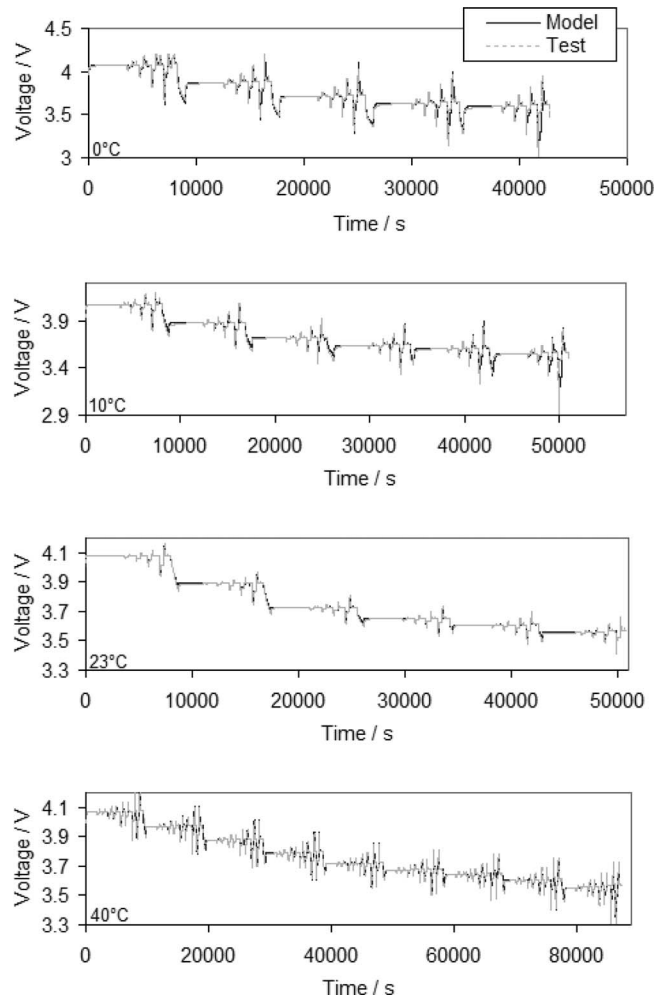


Figure A-2. Voltage data in the considered pulse tests and the associated model fit.

List of Symbols

Abbreviations

AM	Active materials
ACC	Aluminum Current Collector
GCC	Graphite Current Collector
EV	Electric Vehicle

Symbols

A_c	Area of the collector-electrode contact (m^2)
a_i	Polynomial coefficients
b	Bruggeman constant
C^{eff}	Specific heat capacity of the cell ($J\ Kg^{-1}\ K^{-1}$)
c	Molar concentration of lithium ($mol\ m^{-3}$)
$c_{s,av}$	Average solid concentrations ($mol\ m^{-3}$)
D	lithium diffusion coefficient ($m^2\ s^{-1}$)
$D_{e,i}^{eff}$	Electrolyte effective diffusion coefficient ($m^2\ s^{-1}$)
dQ_s	Irreversible Loss in Capacity per cycle (Ah)
$\bar{d}Q_s$	Dimensionless Capacity Loss per cycle
E_{cell}	Cell voltage (V)
F	Faraday 's number 96485 ($C\ mol^{-1}$)
f_{\pm}	Electrolyte activity coefficient
h_{cell}	Height of the pouch cell (m)
I	Cell current (A)
i	Current density ($A\ m^{-2}$)
$i_{0,Li}$	Exchange current density for lithium plating ($A\ m^{-2}$)
J	2D current source in the current collectors ($A\ m^{-2}$)
j^m	Intercalation current density normal to the surface of the particles ($A\ m^{-2}$)
j^{side}	Side reaction current density normal to the surface of the particles ($A\ m^{-2}$)
j_0^m	Exchange current density for the main intercalation reaction ($A\ m^{-2}$)
j_0^{side}	Exchange current density for the side reaction ($A\ m^{-2}$)
k_0^m	Reaction rate coefficient for the main intercalation current
L	Thickness (m)
M_{SEI}	Molecular weight of the SEI layer ($Kg\ mol^{-1}$)
N_{cycle}^{cst}	Number of extrapolation cycles
N^+	Cation flux in the electrolyte phase ($mol\ s^{-1}\ m^{-2}$)
N^-	Anion flux in the electrolyte phase ($mol\ s^{-1}\ m^{-2}$)
n_{layer}	Number of cell sandwiches
\dot{Q}_{rxn}	Heat generation due to reaction overpotential (W)
\dot{Q}_{rev}	Heat generation due to entropic effects (W)
\dot{Q}_{ohm}	Heat generation due to ohmic losses (W)
Q_s	Total irreversible loss of capacity (Ah)
\bar{Q}_s	Total dimensionless capacity loss
\bar{q}_s	Volume average concentration flux in the particles ($mol\ m^{-2}$)
q_s	Concentration flux in the particles ($mol\ m^{-2}$)
R	Universal gas constant ($J\ mol^{-1}\ K^{-1}$)
R_{lumped}	Lumped ohmic resistance (Ω)
R_{SEI}	Resistance of the solid electrolyte interface ($\Omega\ m^2$)
r_p	Active material particle radius (m)
r	Particle radial dimension
S_a	Surface area of active material per volume of electrode (m^{-1})
T	Temperature (K, °C)
t	Time (s)
t^+	Electrolyte Li^+ transference number
U_{eq}	Equilibrium potential (V)
v^+	Number of moles of cation in 1 mole of electrolyte salt
v^-	Number of moles of anion in 1 mole of electrolyte salt
W_{tab}	Width of the cell tabs (m)
z^+	lithium ion charge number
z^-	Electrolyte salt anion charge number

Greek

α	Anodic charge transfer coefficient
δ_{SEI}	SEI film thickness (m)
η^m	Activation overpotential for the main intercalation current (V)
η^s	Activation overpotential for the side reaction current (V)
η^p	Activation overpotential for lithium plating (V)
θ	Dimensionless electrode lithium concentration/stoichiometric coefficient
κ	Electric/Ionic conductivity ($S\ m^{-1}$)
λ_p^{eff}	In-Plane thermal conductivity ($W\ m^{-1}\ K^{-1}$)
ρ_{SEI}	Mass density of the solid electrolyte interface ($Kg\ m^{-3}$)
ρ_{cell}	Mass density of the cell ($Kg\ m^{-3}$)
ϕ_e	Electrode Porosity
φ	Electric potential in the electrode (V)

Operators

d	Ordinary differential
∂	Partial differential
∇	Gradient

Subscript

av	Average molar lithium concentration
ch	Charging conditions
dis	Discharge conditions
eq	Equilibrium conditions
e	Electrode Electrolyte phase
neg	Negative Electrode
pos	Positive Electrode
SEI	Solid Electrolyte Interface
surf	Surface molar lithium concentration
sep	Separator
s	Electrode Solid Phase
x'	Component of the vector in the x' direction
y'	Component of the vector in the y' direction
0	Initial / reference

Superscript

eff	Effective property
k	Number of the electrochemical subdomain in the cell
m	Main intercalation reaction
nc	Negative collector
pc	Positive collector
ref	Reference value
sat	Saturation level
s	Side reaction

References

1. M. Doyle, T. F. Fuller, and J. Newman, *J. Electrochem. Soc.*, **140**(6), (1993).
2. T. F. Fuller, M. Doyle, and J. Newman, *J. Electrochem. Soc.*, **141**(1), (1994).
3. M. A. Keyser, A. Pesaran, M. Mihalic, J.-S. Yu, S.-R. Kim, M. Alamgir, and D. Rivers, "Thermal Characterization of Advanced lithium-Ion Polymer Cells," *Third Advanced Automotive Battery Conference*, June 2003.
4. U. S. Kim, J. Yi, C. B. Shin, T. Han, and S. Park, *Journal of Power Sources*, **196**, 5115 (2011).
5. J. Liu, M. Kunz, K. Chen, N. Tamura, and T. J. Richardson, *J. Phys. Chem. Lett.*, **1**, 2120 (2010).
6. L. Dimesso, C. Spanheimer, S. Jacke, and W. Jaegermann, *J. Power Sources*, **196**, 6729 (2011).
7. M. S. Yazici, D. Krassowski, and J. Prakash, *Journal of Power Sources*, **141**, 171 (2005).
8. S. K. Marthia, J. O. Kiggans, J. Nanda, and N. J. Dudney, *J. Electrochem. Soc.*, **158**(9), A1060 (2011).

9. Dai, Hongli. 2005. High performance lithium or lithium ion cell. Patent 6699623, filed on 10/06/2000, and issued on March 2, 2004.
10. L. Song and J. W. Evans, *J. Electrochem. Soc.*, **147**(6), 2086 (2000).
11. J. B. Gerschler, F. N. Kirchoff, H. Witzhausen, F. E. Hust, and D. U. Sauer, *IEEE*, **978**, 295 (2009).
12. Y. Inui, Y. Kobayashi, Y. Watanabe, Y. Watase, and Y. Kitamura, *Energy Conversion and Management*, **48**, 2103 (2007).
13. Y. Chen and J. W. Evans, *J. Electrochem. Soc.*, **140**(7), 1833 (1993).
14. Y. Chen and J. W. Evans, *J. Electrochem. Soc.*, **143**, 2708 (1996).
15. Y. Chen and J. W. Evans, *J. Electrochem. Soc.*, **141**, 2947 (1994).
16. D. R. Baker and M. W. Verbrugge, *J. Electrochem. Soc.*, **146**(7), 2413 (1999).
17. J. N. Harb and R. M. Lafollette, *J. Electrochem. Soc.*, **146**(3), 809 (1999).
18. J. N. Harb, "The Influence of Current Distribution on Battery Design and Performance," *215th ECS Meeting* (2009).
19. K. H. Kwon, C. B. Shin, T. H. Kang, and C.-S. Kim, *Journal of Power Sources*, **163**, 151 (2006).
20. U. S. Kim, C. B. Shin, and C. Kim, *Journal of Power Sources*, **189**, 841 (2009).
21. R. E. Gerver and J. P. Meyers, *J. Electrochem. Soc.*, **158**(7), A835 (2011).
22. G.-H. Kim, K. Smith, K.-J. Lee, S. Santhanagopalan, and A. Pesaran, *J. Electrochem. Soc.*, **158**(8), A955 (2011).
23. V. Srinivasan and C. Y. Wang, *J. Electrochem. Soc.*, **150**(1), A98 (2003).
24. J. N. Reimers, *Journal of Power Sources*, **158**, 663 (2006).
25. M. Fleckenstein, O. Bohlen, M. A. Roscher, and B. Bäker, *Journal of Power Sources*, **196**, 4769 (2011).
26. G. Ning and B. N. Popov, *J. Electrochem. Soc.*, **151**(10), A1584 (2004).
27. P. Ramadass, B. Haran, P. M. Gomadam, R. white, and B. Popov, *J. Electrochem. Soc.*, **151**(2), A196 (2004).
28. V. R. Subramanian, J. A. Ritter, and R. E. White, *J. Electrochem. Soc.*, **148**, (2001).
29. V. R. Subramanian, V. D. Diwakar, and D. Tapriyal, *J. Electrochem. Soc.*, **152**, (2005).
30. Q. Zhang and R. E. White, *Journal of Power Sources*, **165**, 880 (2007).
31. <http://www.comsol.com/>.
32. PSE, "Material safety data sheet KOKAM superior lithium polymer batteries," 2009, available online <http://www.pse.nl>.
33. S. G. Stewart, V. Srinivasan, and J. Newman, *J. Electrochem. Soc.*, **155**(9), A664 (2008).
34. C. X. Ding, Y. C. Bai, X. Y. Feng, and C. H. Chen, *Solid State Ionics*, **189**, 69 (2011).
35. P. Yu, B. N. Popov, J. A. Ritter, and R. E. White, *J. Electrochem. Soc.*, **146**(1), 8 (1999).
36. L. O. Valoen and J. N. Reimers, *J. Electrochem. Soc.*, **152**(5), A882 (2005).
37. M. Safari, M. Morcrette, A. Teyssot, and C. Delacourt, *J. Electrochem. Soc.*, **156**(3), A145 (2009).
38. R. D. Perkins, A. V. Randall, X. Zhang, and G. L. Plett, *Journal of Power Sources*, **209**, 318 (2012).
39. R. P. Ramasamy, J.-W. Lee, and B. N. Popov, *Journal of Power Sources*, **166**, 266 (2007).
40. O. Borodin, G. D. Smith, and P. Fan, *J. Phys. Chem. B*, **110**, 22773 (2006).
41. W. Fang, O. J. Kwon, and C.-Y. Wang, *Int. J. Energy Res.*, **34**, 107 (2010).
42. V. R. Subramanian and V. Boovaragavan, *J. Electrochem. Soc.*, **156**(4), A260 (2009).
43. P. Ramadass, B. Haran, R. White, and B. N. Popov, *Journal of Power Sources*, **123**, 230 (2003).
44. P. Arora, M. Doyle, A. S. Gozdz, R. E. White, and J. Newman, *Journal of Power Sources*, **88**, 219 (2000).
45. P. Arora, M. Doyle, and R. E. White, *J. Electrochem. Soc.*, **146**(10), 3543 (1999).
46. K. E. Thomas and J. Newman, *Journal of Power Sources*, **119**, 844 (2003).
47. G. E. P. Box and G. C. Tiao, *Bayesian Inference in Statistical Analysis*, Wiley, ISBN 0-471-57428-7 (1973).
48. J. A. Vrugt, C. J. F. ter Braak, C. G. H. Diks, B. A. Robinson, J. M. Hyman, and D. Higdon, *International Journal of Nonlinear Sciences & Numerical Simulation*, **10**(3), 271 (2009).
49. P. Arora and R. E. White, *J. Electrochem. Soc.*, **145**(10), 3648 (1998).
50. www.kokam.com.